Aeroacoustic Performance of High-lift Airfoil with Slat Cove Fillers

Hasan Kamliya Jawahar*, Syamir Alihan Showkat Ali†, Mahdi Azarpeyvand‡,
University of Bristol, Bristol, United Kingdom, BS8 1TR
and
Carlos R. Ilário da Silva§
Embraer, São José dos Campos, 12227-901, Brazil

Experimental measurements to assess the aerodynamic and aeroacoustic capabilities of 30P30N airfoil fitted with two different types of slat cove filler were carried out at the newly commissioned anechoic wind tunnel at the University of Bristol. The aerodynamic results are presented for lift and drag measurements and mean surface pressure measurements. The aerodynamic results showed insignificant changes between the Baseline and the slat cove filler configurations. The lift-to-drag performance for the slat cove filler configuration was marginally better than that of the Baseline case. The pressure distribution results showed a slight reduction in the suction peak over the main element and the flap for the slat cove filler configurations. The results from the simultaneous surface pressure measurement close to the slat cove region and far-field noise measurements above the slat trailing edge are presented to gain a deeper understanding of the noise generation mechanism of the slat. The far-field noise measurement results showed that significant noise reduction can be achieved by the use of slat cove fillers. The directivity pattern and the overall sound pressure level of the radiated noise have also shown that significant noise reduction can be achieved with the applications of the slat cove fillers.

Nomenclature

c	=	stowed chord length, m
c_s	=	slat chord length, m
C_L	=	lift coefficient
C_D	=	drag coefficient
C_p	=	pressure coefficient, $(\overline{p} - p_\infty)/(0.5\rho U_\infty^2)$
f	=	frequency, Hz
k	=	turbulent kinetic energy, m^2/s^2
l	=	span length, m
$\overline{p}$	=	average pressure, Pa
p'	=	fluctuation surface pressure, Pa
P_{ref}	=	reference pressure ($= 2 \times 10^{-5}$), Pa
P_{rms}	=	pressure root mean squared
p_∞	=	static pressure of the flow, Pa
Re_c	=	chord-based Reynolds number
St_s	=	slat chord-based Strouhal number, $(St_s = f \cdot c_s/U_\infty)$
U, U_∞	=	mean velocity, freestream velocity, m/s
ρ	=	air density, kg/m^3
α	=	angle of attack, $^\circ$
τ	=	time delay, s
Φ_{pp}	=	wall-pressure power spectral density, Pa^2/Hz
$\gamma^2_{p_i p_j}$	=	wall pressure coherence between transducers p_i and p_j
Λ_γ	=	spanwise coherence length, m

*Research Associate, Department of Aerospace Engineering, hasan.kj@bristol.ac.uk
†Senior Lecturer, School of Manufacturing Engineering, Universiti Malaysia Perlis, 02600, Perlis, Malaysia, syamir@unimap.edu.my
‡Reader in Aeroacoustics, Department of Mechanical Engineering, m.azarpeyvand@bristol.ac.uk
§Technology Development Engineer, Embraer, Sáo José dos Campos, Brazil, carlos.ilario@embraer.com.br

I. Introduction

THE increasing popularity of air travel and the expected doubling of passengers every 10 years have made aircraft industry of great economic importance globally. This extensive growth of the aircraft industry constantly demands much more efficient and quieter aircraft than the ones currently in service. The impact noise generated by aircraft during take-off and landing has come under a lot of scrutinies over the past decade especially with the increasing popularity in air travel and expanding airports. Even though the aircraft engine noise has been brought down substantially by the use of high bypass engines the airframe noise remains a major contributor to aircraft noise. In order to reduce these prominent noise sources several passive and active flow control methods have been investigated in the past it includes morphing structures [1–7], porous materials [8–11], surface treatments [12], serrations [13–15] and transverse jets [16]. The high-lift devices namely the slats and flaps are one of the major contributors to airframe noise. Their noise generation mechanism is of both broadband and narrowband in nature. Studies on conventional slat and wing configurations have shown that it mainly comprises of broadband and tonal noise components. Several studies on slat noise have shown several discrete tones at mid-frequency range [17–29]. However, their aeroacoustic mechanism is yet to be fully understood. These tonal peaks decrease with angle of attack but their amplitude decreases with increasing slat gap and overlap [24].

Several experimental and computational studies [30–40] were made over the past decade to reduce the broadband noise arising from the slat cove region by filling the recirculation area within the slat cove gap. The tonal peaks seen in slat noise are due to the vortex shedding at the slat cusp and its impingement on the slat lower surface along with a feed back loop in between them. In order to eliminate this tonal noise and the broadband noise from the shear layer impingement the approach of filling the slat cavity is used. Horne *et al.* from NASA in order to eliminate the unsteady recirculation region within the slat cove tested a solid slat cove filler (SCF) on a Boeing 777-200 semi span model in the NASA Ames 40 by 80 foot Wind Tunnel. The slat cove filler profiles were derived from CFD analysis in order to maintain attached flow on the slat lower surface. From the experiments it was shown that slat cove filler was effective in reducing broadband slat noise upto 4-5 dB [30] that was measured using a microphone phased array. However no aerodynamic measurements were presented in this study. Streertt *et al.* further investigated noise and basic aerodynamics of the SCF setup using trapezoidal wing swept model fitted [31]. The results showed noise reduction to be sensitive to the angle of attack and SCF modification. The SCF modification showed a reduction of 3-5 dB over a wide spectrum. The aerodynamic performance appeared slightly better than the baseline at angles of attack below 20° and stall occurred 2 degrees earlier compared to baseline. The specific reason of the aerodynamic performance loss was not pointed out due to the lack of aerodynamic data such as detailed surface pressure and wake shear layer measurements.

Imamura *et al.* and Ura *et al.* from JAXA showed experimentally and computationally [35, 36] that even though noise reduction can be achieved by the use of SCF, its profile significantly affects the aerodynamic lift characteristics of the three-element airfoil. They tested two SCF profiles that were designed based on the flow field streamlines of angles of attack 0° and 8° on a MDA 30P30N airfoil. Eventhough the results showed a reduction of 5 dB for both the cases they found that the aerodynamic lift characteristics performance were same as that of the baseline for only the SCF profile made from flow field streamlines of angle of attack 8° whereas the SCF profile made from angle of attack 0° stalls prematurely. Tao and Sun [40] in a very recent optimisation study performed several DES simulations using 44 configurations of SCF profile designs aimed to produce maximum lift coefficient for fixed design point with angle of attack of 22° and $Re_c = 9 \times 10^6$. The final optimised SCF profile showed a reduction in noise while maintaining aerodynamic performance.

Several studies [30–40] have been performed on the overall noise reduction capabilities of the slat cove filler. This experimental study presents a detailed aerodynamic performance characteristics such as lift and drag measurements and surface pressure measurements along with high-quality aeroacoustic measurements have also been acquired from state of the art acoustic facility at the University of Bristol. The acoustic results presented show a comprehensive analysis of the performance of 30P30N airfoil fitted with two types of slat cove fillers.

II. Experimental Setup

A. Airfoil Setup

An MDA 30P30N three-element high-lift airfoil with a retracted chord of $c = 0.35$ m and a span of $l = 0.53$ m was manufactured using a computer-aided numerically controlled machine. The geometrical parameters of the high-lift airfoil are shown in Fig. 1 and Table. 1. In order to maintain two-dimensionality within the slat cove and flap cove regions, no brackets were used in the spanwise direction. All the three-elements were held together by steel clamps on the sides of the airfoil. Sandpaper trip (80 grit) with a thickness of $h_t = 0.6$ mm and a width of $w_t = 3$ mm at location $x/c = -0.055$ on the pressure side of the slat surface just upstream of the slat cusp was used to trip the flow and induce turbulent shear layer [19]. The MDA airfoil was also equipped with a large number of static pressure taps (103) placed along the mid-span of the airfoil.

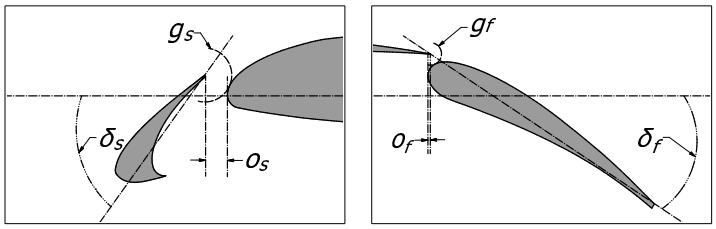

Fig. 1. MDA 30P30N three-element high-lift airfoil geometric parameters.

Table 1. Geometrical parameters in percentage of stowed airfoil chord, $c = 0.35$ m.

Slat chord	c_s	$0.15c$
Main-element chord	c_{me}	$0.83c$
Flap chord	c_f	$0.3c$
Slat deflection angle	δ_s	30°
Flap deflection angle	δ_f	30°
Slat gap	g_s	2.95%
Flap gap	g_f	1.27%
Slat overhang	o_s	−2.5%
Flap overhang	o_f	0.25%

B. Wind-Tunnel Setup

The aerodynamic measurements were carried out in the large low-speed closed-circuit wind tunnel at the University of Bristol. It has an octagonal working area of 2.1 m × 1.5 m × 2 m and a contraction ratio of 3:1. The wind-tunnel is capable of a maximum velocity up to 60 m/s with typical turbulence intensity levels as low as 0.25%. The aeroacoustic measurements were carried out at the University of Bristol Aeroacoustic Facility. It is a closed circuit open-jet anechoic wind tunnel with a nozzle exit of 0.5 m × 0.775 m and a contraction ratio of 8.4:1. The wind tunnel is capable of velocities up to 40 m/s with turbulence levels as low as 0.25% [41].

1. Lift and Drag Measurements Setup

The lift and drag measurements were carried out using an AMTI OR6-7-2000 force platform from Advanced Mechanical Technology Inc., mounted at the base of the side arms that held the airfoil set-up. The data were collected through a 16-bit A/D card for a period of 16 seconds at sampling frequency of 2000 Hz, which deemed sufficient enough from an uncertainty analysis of the collected data.

2. *Static Pressure Measurements Setup*

MicroDaq pressure scanners manufactured by Chell Instruments were used for static surface pressure measurements. Two scanners equipped with 32 channels were used to measure the surface pressure. The scanners have a full scale measuring capacity of 1 Psi with system accuracy of ±0.05%. The measurements were made with a frequency of 500 Hz and the data was collected for 60 seconds.

3. *Unsteady Pressure Measurements Setup*

FG-3329-P07 transducers from Knowles Electronics were installed on the main-element of the wing to measure the unsteady surface pressure on the MDA airfoil (see Table. 2). This transducer was selected for measurement as it was proven successful in previous experiments carried out by Garcia [42–44] on NACA 0012 airfoil. The transducer has a diameter of 2.5 mm and a height of 2.5 mm with a sensing area of 0.8 mm. The FG-3329-P07 transducer has a manufacture provided sensitivity of 22.4 mV/Pa (45 Pa/V) in the flat region of the transducer response. The transducer sensitivity obtained from the calibration varied between 20.2 mV/Pa and 23.5 mV/Pa. The unsteady surface pressure measurements using FG transducers were carried out for 16 seconds using a sampling frequency of $f = 2^{16}$ Hz.

Table 2. Pressure transducer locations on the MDA 30P-30N airfoil.

Main-Element	No.	x (mm)	z (mm)
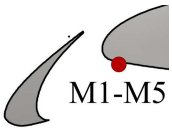	M1	22.414	277
	M2	22.414	280.6
	M3	22.414	288.4
	M4	22.414	301.4
	M5	22.414	319.6

4. *Slat cove-filler Design*

As part of the noise reduction study of the MDA airfoil, a slat cove-filler (SCF) was designed using a similar strategy introduced by Imamura *et al.* [35, 36] for experimentation purposes. Initially, preliminary RANS steady-state simulation for the Baseline case was performed at the angle of attack $\alpha = 8°$ and the slat shear layer trajectory with high TKE was used to define the shape of the SCF profile. Another configuration with a Half SCF (H-SCF) was also considered, which exhibits good aerodynamic and noise reduction properties as shown computationally by Tao [40]. Both the slat cove-fillers and the flap cove-fillers (FCF) were manufactured using 3D printing technology and was manufactured in four different sections that could be slid along the span of the slat and flap cove. The solid SCF is fitted with 6 pressure taps along the mid-span of the wing for surface pressure measurements and the solid FCF is fitted with 3 pressure taps.

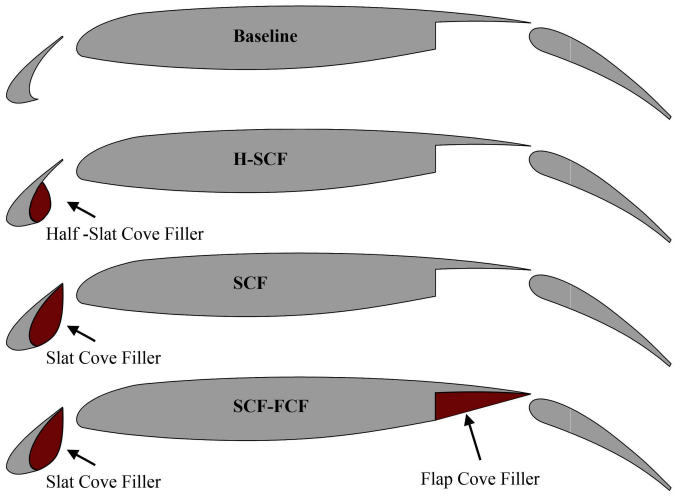

Fig. 2. MDA 30P30N Baseline airfoil fitted with half-slat cove filler (H-SCF), slat cove filler (SCF) and flap cove filler (FCF).

5. *Acoustic measurements and instrumentations*

The schematic of the experimental setup of the high-lift airfoil for the aeroacoustic measurements is shown in Fig. 3. The far-field noise measurements were carried out using an array of 22 G.R.A.S. 40PL piezoelectric free-field microphones distributed over a circular arc at a radius of 1.75 m from the slat trailing edge. The microphone array covered a range of polar angles between 35° to 140°, with a regular interval of 5° (see Fig. 3). The microphone has a flat frequency response at frequencies from 10 Hz to 10 kHz, with a dynamic range of 142 dB. The far-field noise spectra were computed for 16 seconds using a sampling frequency of $f = 2^{16}$ Hz. The acoustic data were recorded at a wide range of flow velocities of up to 40 m/s. The sound pressure level (SPL) spectrum can be calculated using,

$$\mathrm{SPL} = 20 \cdot \log 10\left(\frac{P_{rms}}{P_{ref}}\right), \tag{1}$$

where P_{rms} is the root-mean-squared of the acoustic pressure and P_{ref} is the reference pressure at 20 μPa. The power spectrum of the acoustic pressure signal is corrected to a reference distance of 1 m.

The overall sound pressure level (OASPL) are obtained using,

$$\mathrm{OASPL} = 10 \cdot \log 10\left[\frac{\int \mathrm{PSD}(f)\,\mathrm{d}f}{P_{ref}^2}\right], \tag{2}$$

where PSD is the power spectral density based on the unsteady pressure $p^{'}$ (where $p^{'} = p - p_{mean}$). The resolved frequency f ranges from 100 Hz to 32 kHz.

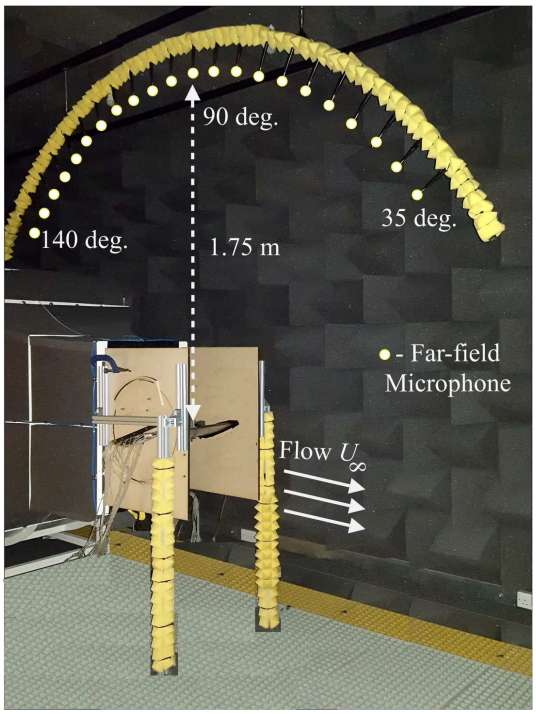

Fig. 3. Test model mounted in the aero-acoustic wind tunnel.

III. Results and Discussion

A. Aerodynamic Measurements

The airfoil was tested for a range of angles of attack from, $\alpha = 0°$ to $18°$ freestream velocities 20, 30, 40 and 47 m/s. The tested configurations were the Baseline, Half-slat cove-filler (H-SCF), Slat cove-filler (SCF) and Slat cove-filler along with Flap cove-filler (SCF-FCF), as shown in Fig. 2. The MDA airfoil was equipped with 103 pressure taps to accurately capture the surface pressure distribution.

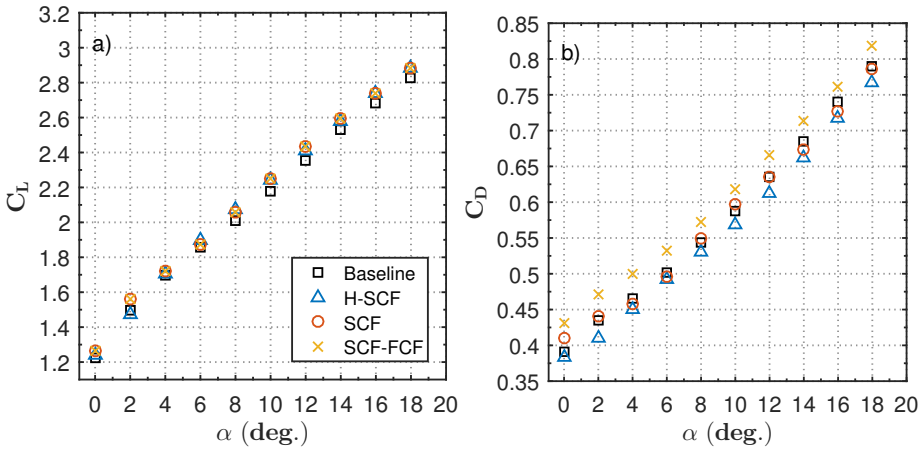

Fig. 4. Lift and Drag coefficient for the 30P30N airfoil with various cove fillers at chord based Reynolds number $Re_c = 9.3 \times 10^5$.

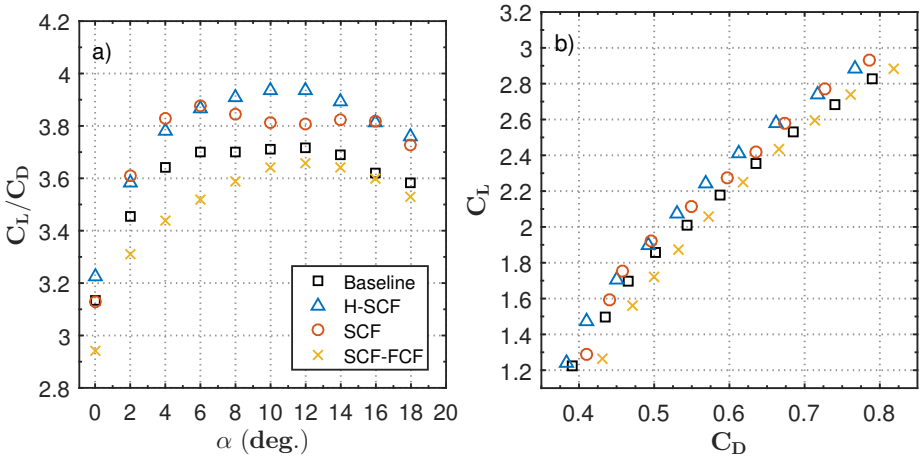

Fig. 5. Lift-to-drag ratio and the drag polar plots for the 30P30N airfoil with various cove fillers at chord based Reynolds number $Re_c = 9.3 \times 10^5$.

1. Aerodynamic lift measurements

The aerodynamic lift and drag measurements for the 30P30N airfoil with different cove fillers at a freestream velocity of $U_\infty = 40$ m/s corresponding to a chord based Reynolds number of $Re_c = 9.3 \times 10^5$ are presented in Fig. 4. The tests were carried for angles of attack ranging from $\alpha = 0°$ to $18°$ with a $\Delta\alpha = 2°$. The lift and drag coefficient (C_L and C_D) for the Baseline, H-SCF, SCF and the SCF-FCF configurations are presented in Fig. 4. The C_L results show an insignificant difference among the cases for all the presented angles of attack. The C_D results show that the SCF-FCF configuration produced the highest C_D for all the angles of attack compared to the Baseline and all the other configurations. The H-SCF configuration has the least C_L relative to the Baseline and the other configurations for all the tested angle of attack. The SCF has C_L values same as that of the Baseline.

The results for the lift-to-drag coefficient ratio and the drag polar curves for the Baseline, H-SCF, SCF and the SCF-FCF configurations are presented in Fig. 5. The lift-to-drag coefficient (C_L/C_D) results show a significant difference

among the presented configurations. The H-SCF produces a higher C_L/C_D relative to the Baseline and the SCF-FCF configuration. For the SCF configuration with a large cove filler, the C_L/C_D values remain the same as that of the best performing H-SCF between $\alpha = 0°$ to $8°$ and $16°$ to $18°$. The highest change in C_L/C_D value relative to the Baseline was seen for the H-SCF between $\alpha = 8°$ and $14°$ with an average $\Delta C_L/C_D \approx 0.214$ ($\approx 5.4\%$). The largest difference in C_L/C_D was found between the H-SCF and SCF-FCF, $\Delta C_L/C_D = 0.358$ at $\alpha = 6°$. The drag polar curve results in Fig. 5b shows the C_L versus the C_D for increasing angles of attack from left to right. The results clearly show relative to the Baseline the H-SCF has the least drag for all the presented angles of attack, while the SCF-FCF has the highest drag compared to all the configurations.

2. *Pressure coefficient distribution*

The pressure coefficient C_p distribution calculated from the mean surface pressure measurements acquired along the mid-span of the Baseline case, for the tested chord-based Reynolds numbers $Re_c = 4.9 \times 10^5, 7.0 \times 10^5, 9.3 \times 10^5$ and 1.1×10^6 at the angle of attack $\alpha = 12°$ is presented in Fig. 6. The results show that the changes in C_p distribution over the slat and main-element are insignificant for the tested Reynolds numbers. An increase only in the order of 1.5% on the suction peak (C_p) of the main-element was observed for $Re_c = 9.3 \times 10^5$ relative to $Re_c = 4.9 \times 10^5$, whereas the changes on the suction peak of the flap were up to 15% higher for $Re_c = 9.3 \times 10^5$ and 20% higher for $Re_c = 1.1 \times 10^6$ relative to the $Re_c = 4.9 \times 10^5$. Valarezo [45,46] showed that the effects of Reynolds number on the lift of multi-element airfoil was very evident for flow conditions below $Re_c = 4 \times 10^6$. They also showed a considerable increase in the maximum lift between $Re_c = 2 \times 10^6$ and 9×10^6 at a Mach number of 0.2. The effects of Reynolds number and its significance on the lift of high-lift airfoil was also shown by Chin *et al* [47] and they also discussed the increased effect of Reynolds number on the suction peak of the flap.

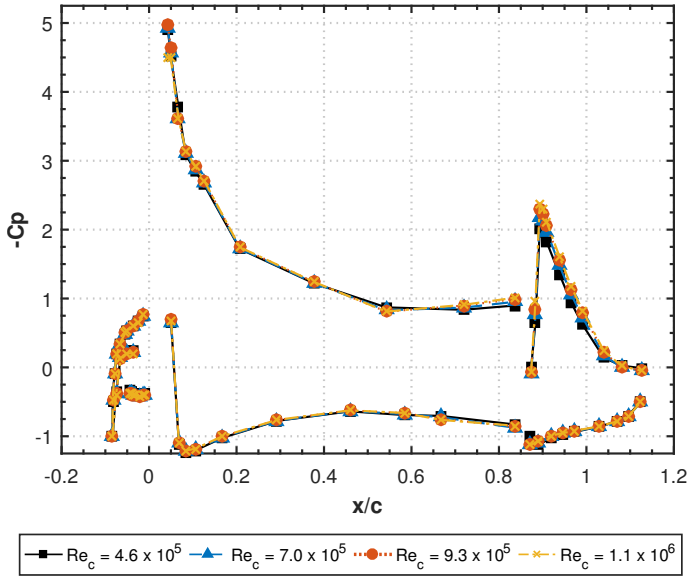

Fig. 6. Coefficient of pressure distribution over 30P30N Baseline airfoil at angle of attack $\alpha = 12°$.

The pressure coefficient distribution for the Baseline at the tested angles of attack $\alpha = 12°, 14°, 16°$ and $18°$ are presented in Fig. 7. The change in C_p distribution is evident especially on the suction side of the main-element as the angle of attack is increased. The loading on the slat and main-element increases with the increase in angle of attack. The increased suction peak on the main-element at higher angles of attack is due to the higher velocity from the increased mass flow through the slat gap as the angle of attack is increased. The suction peak on the upper surface of the main-element increases up to $\approx 1\%$, 6.8% and 14% for $\alpha = 14°$, $16°$ and $18°$ relative to $\alpha = 12°$. The suction peak on the upper surface of the flap increases up to $\approx 5.6\%$ for $\alpha = 18°$ relative to $\alpha = 12°$.

Figures 9 and 10 show the pressure coefficient C_p for the Baseline, H-SCF, SCF and SCF-FCF configurations. The results in Fig. 9 show that the modifications on the slat such as H-SCF/SCF affect the suction peak on the main-element of the airfoil. The Baseline has the highest suction peak for both the presented angles of attack. The C_p suction peak on the main-element at location $x/c = 0.043$ was reduced by $\approx 12\%$ at $\alpha = 12°$ and $\approx 14\%$ for the H-SCF, SCF and

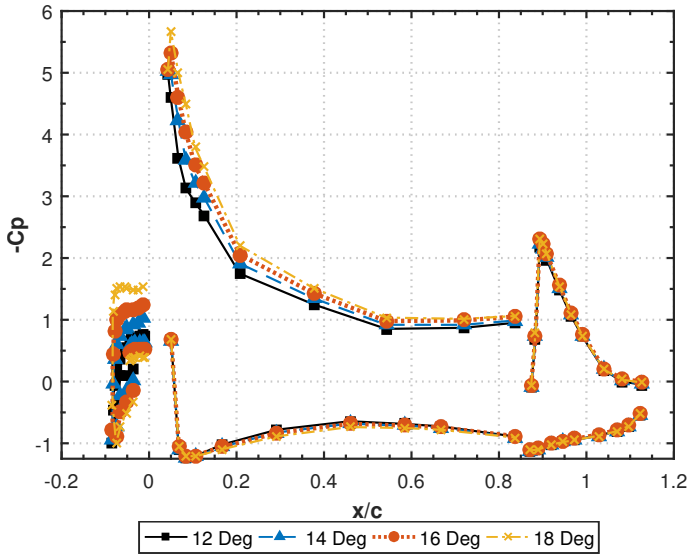

Fig. 7. Pressure coefficient distribution over 30P30N Baseline airfoil for a freestream velocity of $U_\infty = 30$ m/s, $Re_c = 7.0 \times 10^5$.

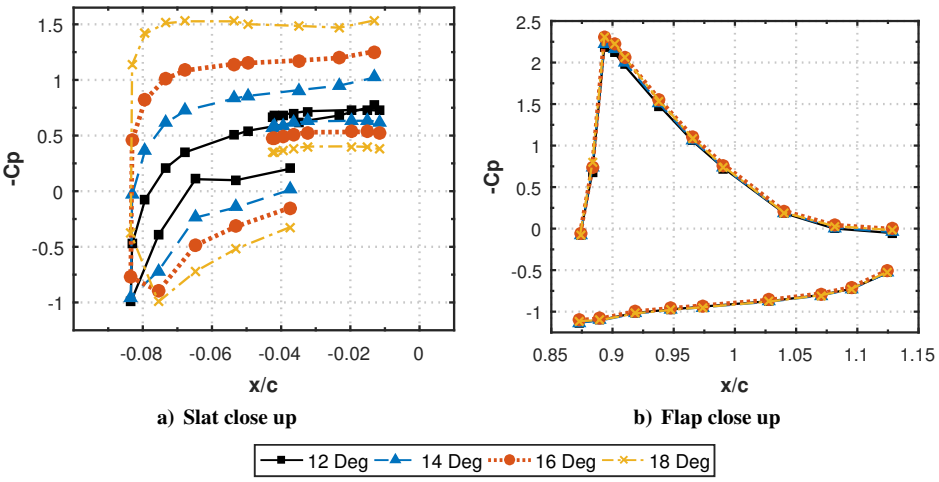

Fig. 8. Pressure coefficient distribution over 30P30N Baseline airfoil around the slat and flap region for a freestream velocity of $U_\infty = 30$ m/s, $Re_c = 7.0 \times 10^5$.

SCF-FCF cases relative to the Baseline. The results for the slat in Fig. 10 show that the C_p on the pressure side changes quite significantly for the H-SCF/SCF configurations as the angle of attack is increased. The suction peak near the slat cusp is decreased for the H-SCF/SCF relative to the Baseline by up to 40% for the angle of attack $\alpha = 12°$. This is due to the absence of sudden pressure gradient and the increased velocity due to the streamlined profile of the cove fillers. The C_p measurements over the flap for the presented angles of attack remains unchanged for the Baseline and H-SCF/SCF configuration. The results for the SCF-FCF configuration show an increase of up to $\approx 20\%$ in the C_p on the pressure side of the main-element at the location of the flap cove filler between $x/c \approx 0.6$ and 0.8. The SCF-FCF results over the flap at the suction peak location $x/c = 0.90$ is $\approx 5\%$ higher for the SCF-FCF configuration relative to the Baseline. Previous studies on MDA airfoil has shown that the confluent boundary layers arising from the slat and main-element play a major role in the delayed separation over the flap.

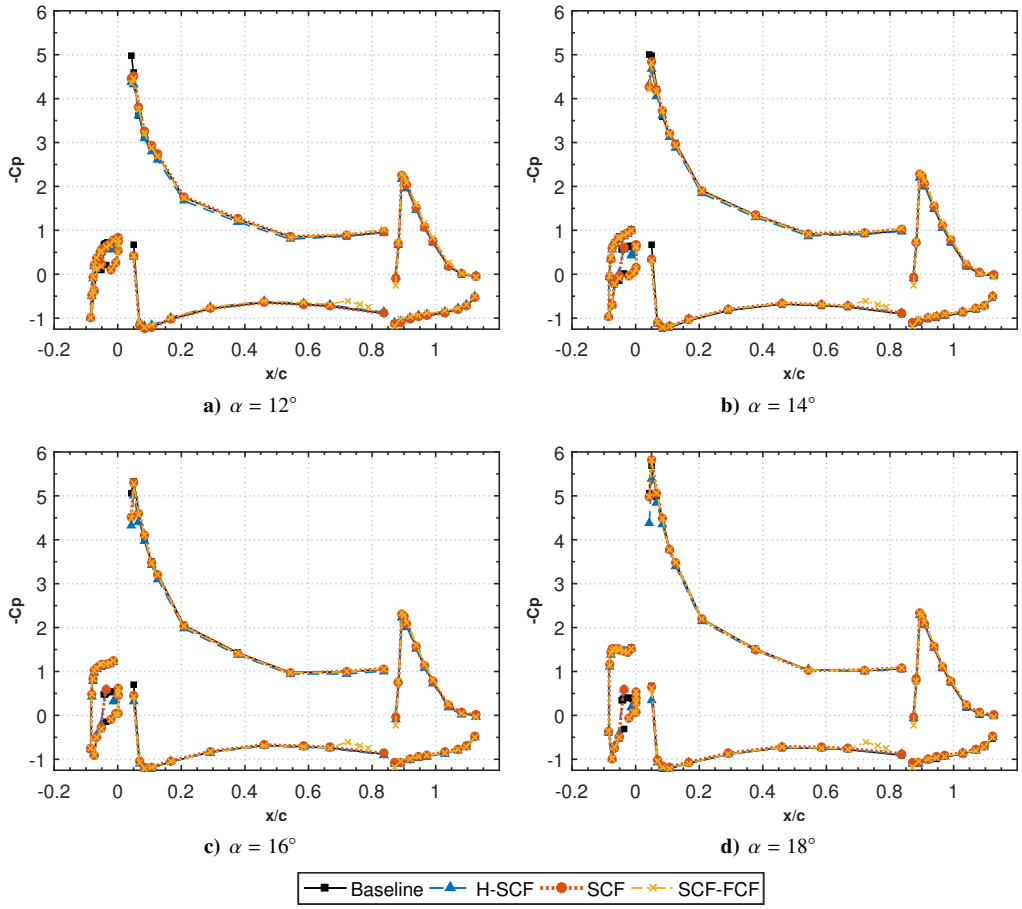

Fig. 9. Pressure coefficient distribution over 30P30N airfoil with slat modifications, for a freestream velocity of $U_\infty = 30$ m/s, $Re_c = 7.0\times10^5$.

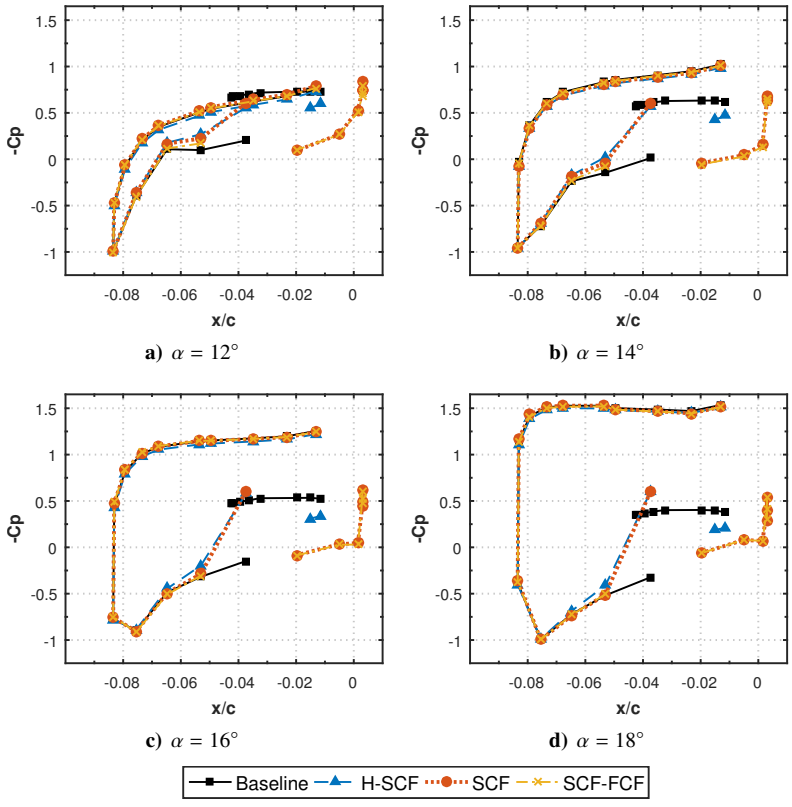

Fig. 10. Pressure coefficient distribution over 30P30N airfoil with slat modifications, for a freestream velocity of $U_\infty = 30$ m/s, $Re_c = 7.0 \times 10^5$.

B. Near-field spectral levels

The unsteady surface pressure measurements were acquired at various spanwise location on the surface of the main-element of the high-lift airfoil. The measurements were carried out using 5 flush-mounted pressure transducers, which are detailed in Table. 2. The data were acquired for 32 seconds and sampled at 40 kHz. Even though the measurements were completed for angles of attack $\alpha = 12°, 14°, 16°$ and $18°$ for the purpose of brevity the results here are presented only for angles of attack $\alpha = 14°$ and $18°$. The presented wall-pressure spectra results were obtained by discrete power spectral density (PSD) of the pressure signals using Hanning window and the acquired data were averaged for 200 times to yield a frequency resolution of $\Delta f = 6.25$ Hz. From the aeroacoustic study carried out by Murayama *et al.* [34], it was seen that the flush-mounted pressure transducers on the main-element were sufficient enough to clearly capture the narrowband and broadband spectra of the vortical fluctuations within the slat cove region. The results from the unsteady surface pressure measurements from the transducer M1 at the leading edge of the main-element are shown in Fig. 11. The wall pressure fluctuation spectra results for the Baseline in Fig. 11 show distinct narrowband peaks for all the tested angles of attack with varying intensities. Three distinct tonal peaks in the mid-range frequency were observed for $\alpha = 14°$ with frequencies $f_1 = 485$ Hz, $f_2 = 971$ Hz and $f_3 = 1485$ Hz corresponding to a slat-chord based Strouhal number ($St_s = f \cdot c_s / U_\infty$) of $St_s = 0.88, 1.59, 2.37$ respectively. At the angle of attack $\alpha = 18°$ multiple peaks with higher intensities are observed with the first three frequencies $f_1 = 512$ Hz, $f_2 = 990$ Hz and $f_3 = 1418$ Hz corresponding to a slat-chord based Strouhal number of $St_s = 0.89, 1.83, 2.48$ respectively. The other narrowband tonal peaks observed shows relationship between themselves which must be further analyzed using higher spectral order analysis. The tonal peaks occurring at even intervals show higher energy compared to the peaks occurring at odd intervals and the even peaks show harmonic relation between themselves for example peak four $f_4 = 1982$ Hz is also approximately equal to $2f_2$.

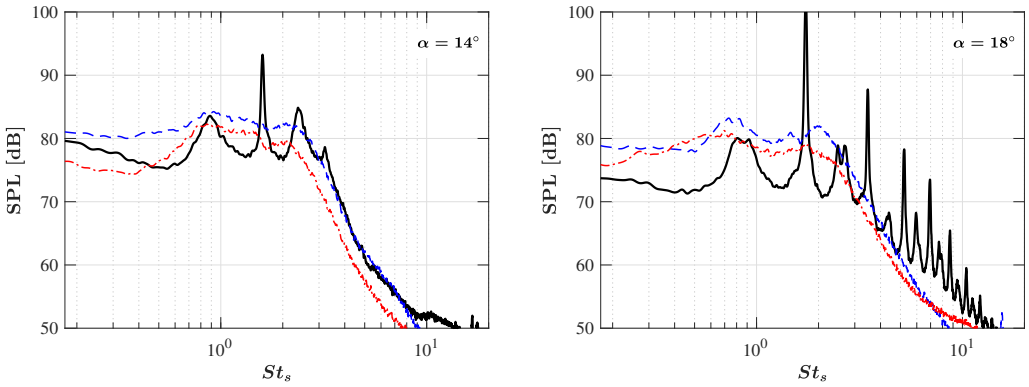

Fig. 11. Near-field noise spectra for the surface transducer M1 ($x = 22.414$ mm) at the main-element leading-edge of a 30P30N airfoil with slat modifications, for a freestream velocity of $U_\infty = 30$ m/s, $Re_c = 7.0 \times 10^5$, for Baseline —, H-SCF – – – and SCF – · –.

The results in Fig. 11 evidently show that the use of H-SCF and SCF configuration for both the presented angles of attack eliminates the tonal peaks, which was observed for the Baseline case. At the angle of attack $\alpha = 14°$, for the H-SCF configuration, the wall pressure spectra show an increase of up to 5 dB compared to the Baseline case at low-mid frequency range $f < 1428$ Hz ($St_s \approx 2.5$). In the case of the SCF at $\alpha = 14^circ$ a reduction of up to 5 dB relative to the Baseline case at low-frequency range can be observed $f < 512$ Hz. At the angle of attack, $\alpha = 18°$ both the H-SCF and SCF shows a broadband increase of up to 9 dB at low-mid frequency range $f < 1428$ Hz ($St_s \approx 2.5$). Moreover, the presence of the half-cavity for the H-SCF configuration gives rise to two spectral humps that are evidently seen in the case of $\alpha = 18°$ at low frequency range $f = 342$ and 1143 ($St_s = 0.6$ & 2) The SCF configuration at $\alpha = 14°$ also shows an overall reduction of 2 dB compared to the Baseline and H-SCF configuration at mid-high frequency range (see Fig. 11). At the angle of attack $\alpha = 18°$ a reduction of up to 3 dB can be observed at a high-frequency range $f > 2857$ Hz.

C. Far-field spectral levels

Far-field noise measurements were carried out in order to assess the noise generated from the Baseline, H-SCF, and SCF configurations. The sound pressure level measured from a far-field microphone at 90° above the slat trailing edge for the angle of attack $\alpha = 14°$ and $18°$ at the free-stream velocity of $U_\infty = 30$ m/s is shown in Fig. 12. The results show that the background noise of the aeroacoustic facility is well below the high-lift airfoil noise levels. While the results for the baseline 30P30N airfoil show the discrete narrowband peaks, typical of the noise signature from

such high lift devices, the far-field noise results of the H-SCF and SCF configuration do not demonstrate such tonal behavior. The SCF configuration at the angle of attack $\alpha = 18°$ clearly shows a reduction in the noise levels over the entire frequency range. Significant noise reduction of up to 8 dB at low to mid-frequency range $f < 2857$ Hz ($St_s < 5$) are observed for the SCF configuration compared to the Baseline and H-SCF cases. At the angle of attack $\alpha = 14°$ the SCF configuration showed an overall reduction in the near-field spectral level up to 2 dB (see Fig. 11), however, this reduction observed at the near-field measurements is not seen in the far-field measurements. In the case of angle of attack $\alpha = 18°$ both the H-SCF and SCF configuration showed an increase in low-mid frequency range in the near-field spectral level up to 5 dB (see Fig. 11) but in the far-field measurements, the SCF configuration shows a decrease of up to 9 dB in the low-mid frequency range. From these observations, it can be concluded that the increased spectra in the near-field measurements are due to the non-propagating hydrodynamic energy field within the slat cove and main element region.

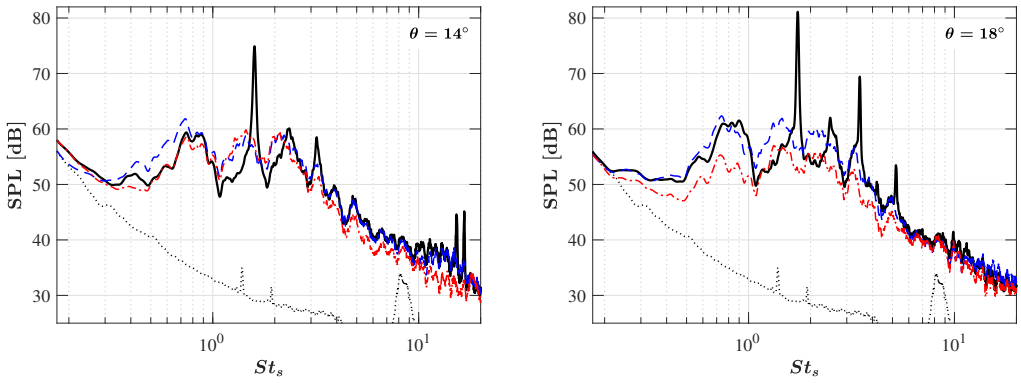

Fig. 12. Far-field noise spectra for microphone at 90° and 1.75 m above the slat trailing edge for a freestream velocity of $U_\infty = 30$ m/s, $Re_c = 7.0 \times 10^5$, for Baseline —, H-SCF – – – and SCF – · – and Background · · · · .

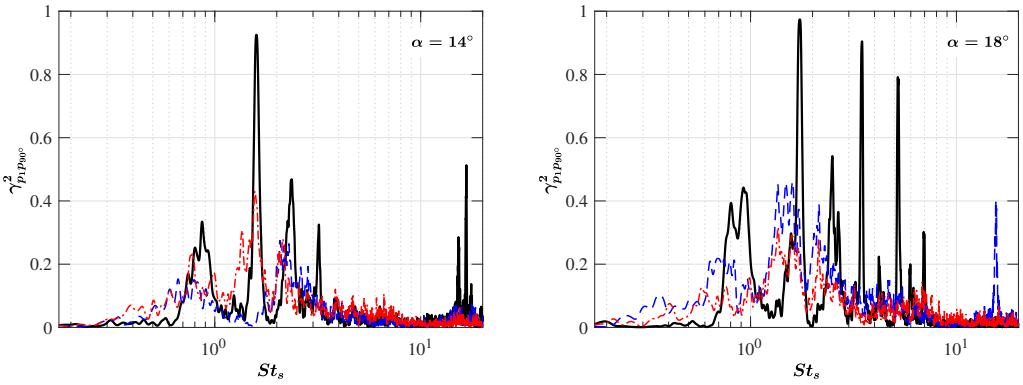

Fig. 13. Coherence between the reference transducer M1 and the far-field micrphone 90° above the trailing edge, for Baseline —, H-SCF – – – and SCF – · –.

To further understand the intensity of the noise radiated to the far-field and isolate the non-propagating hydrodynamic field, coherence between the surface pressure transducer M1 and the far-field microphone placed at 90° above the slat trailing-edge were carried out. The coherence was calculated using the following equation,

$$\gamma^2_{p_i p_j}(f) = \frac{|\,\Phi_{p_i p_j}(f)\,|^2}{\Phi_{p_i p_i}(f)\Phi_{p_j p_j}(f)} \quad \text{for } p_i = \text{ M1 and } p_j = \text{M}_{90°}, \tag{3}$$

where M1 is the reference surface pressure transducer and $M_{90°}$ is the far-field microphone at 90° above the slat trailing edge. The near- to far-field coherence results are presented in Fig. 13. The results show high coherence at all tonal peaks previously observed in the far-field measurements. The H-SCF and SCF cases show low coherence over the entire frequency range. However, a noticeable spectral hump between frequencies 571 Hz $< f <$ 2285 Hz ($1 < St_s < 4$) with maximum coherence values up to $\gamma^2_{p_i p_{90°}} = 0.6$ for the H-SCF and SCF cases are seen at angle of attack $\alpha = 18°$. This increased coherence spectral hump shows a feature that was not seen in both the near-field and far-field sound pressure level measurements.

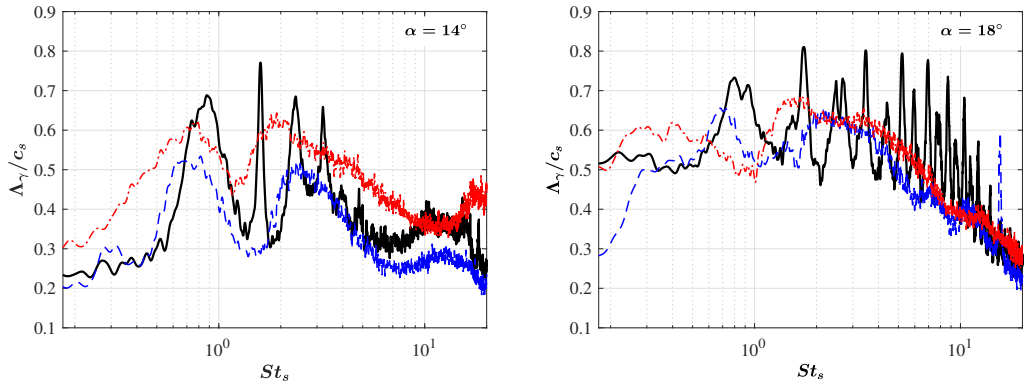

Fig. 14. Spanwise coherence length scales based on the unsteady surface pressure measurement for Baseline —, H-SCF - - - and SCF – · –.

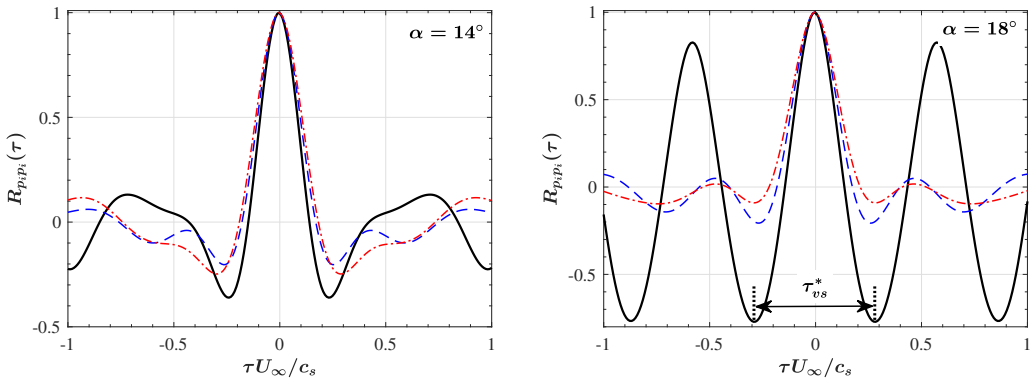

Fig. 15. Auto-correlation of the surface pressure fluctuations at the near-field transducer location M1 for Baseline —, H-SCF - - - and SCF – · –.

In order to estimate the noise generated through the interaction of advecting pressure in the vicinity of the airfoil, the spanwise correlation length of the wall pressure fluctuations were calculated. The spanwise correlation length of the flow structures and the local hydrodynamic field can be calculated using the following equation,

$$\Lambda_\gamma(f) = \int_0^\infty \gamma_{p_ip_j}(f, \Delta z) d\Delta z, \tag{4}$$

$$\gamma^2_{p_ip_j}(f) = \frac{|\ \Phi_{p_ip_j}(f)\ |^2}{\Phi_{p_ip_i}(f)\Phi_{p_jp_j}(f)} \quad \text{for } p_i = M1 \text{ and } p_j = M1, M2, M3, M4, M5. \tag{5}$$

where Δz is the distance between the pressure transducers in the spanwise direction and the length scale (Λ_γ) as a function of frequency is calculated using the spanwise coherence results (γ) between the surface pressure transducers and are presented in Fig. 14. For the angle of attack $\alpha = 14°$, the results show two distinct spectral humps for the length scales for all the configurations. The Baseline and the H-SCF results follow the same trend with similar length scales but with the absence of the tonal peaks for the H-SCF configuration. The SCF case shows slightly increased length scales relative to the Baseline and the H-SCF. At the angle of attack, $\alpha = 18°$, the three configurations possess the same broadband trend at mid to high-frequencies ($f > 571$ Hz, $St_s > 1$). The length scales show the spectral hump for only the Baseline case at low-frequencies ($f < 571$ Hz, $St_s < 1$). This shows that for the H-SCF configuration, even though the size of the cavity is reduced and the acoustic feedback mechanism that gives rise to the tonal behavior has been eliminated, the spanwise correlation length remains the same as that of the Baseline airfoil.

The auto-correlation were calculated using the unsteady surface pressure, it is defined as,

$$R_{p_ip_i}(\tau) = \frac{\overline{p_i(t+\tau)p_i(t)}}{p^2_{i_{RMS}}}, \tag{6}$$

where p_i is the surface pressure, $p_{i_{RMS}}$ is the surface pressure root mean squared, τ is the time delay and the time average is represented by the overbar. The results of the auto-correlation of the surface pressure at the transducer

location M1 at the angle of attack $\alpha = 14°$ and 18° are presented in Fig. 15, as a function of the normalized time delay $\tau^* = \tau U_\infty / c_s$. For the Baseline, at the angle of attack $\alpha = 14°$ the results exhibit a fast decaying periodic behavior. At the angle of attack $\alpha = 18°$ the results exhibit a slow decaying periodic behavior with a Gaussian shape with a low decay rate, which is suggestive of a strong vortex shedding. At the angle of attack $\alpha = 18°$, the distance between the two peaks in $R_{p_i p_i}(\tau)$ for the Baseline case corresponds to the vortex shedding frequency (τ^*_{vs}). The calculated time delay $\tau^*_{vs} = 0.5711$ corresponds to $St_{vs} = 1.75 \approx f_2 = 990$ Hz, which is the primary peak seen in near-field and far-field power spectral plots (see Figs. 11 and 12) with the highest magnitude. The vortex shedding for the angle of attack $\alpha = 14°$ is not seen distinctly compared to $\alpha = 18°$. This is due to the lower energy of the vortex shedding frequency (see f_2 in Fig. 11) at angle of attack $\alpha = 14°$ (10 dB) compared to $\alpha = 18°$ (25 dB). The results of the H-SCF and SCF cases show a very weak periodic shape that decays instantaneously, indicating the absence of a strong vortex shedding for both the presented angles of attack. Even though the H-SCF configuration has half a cavity slat, its behavior is more similar to that of the SCF than the Baseline case.

D. Directivity

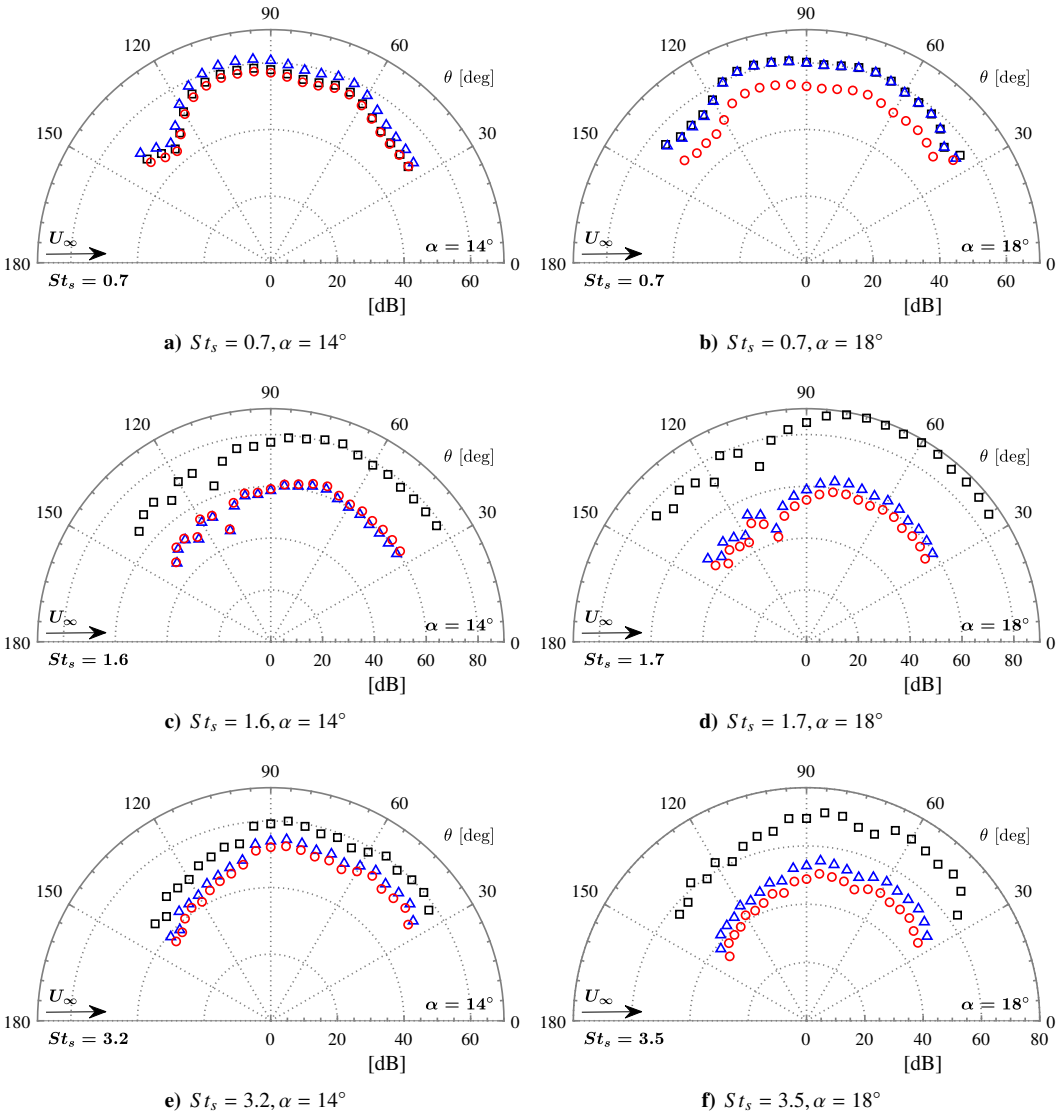

Fig. 16. Directivity for the different configurations at different slat based Strouhal number, for Baseline □, H-SCF △ and SCF ○.

The Far-field directivity plots from the pressure side elevation angles for the Baseline, H-SCF, and SCF configurations at different slat based Strouhal number are presented in Fig. 16. The results are plotted for the angles of attack $\alpha = 14°$ and $18°$, for a free-stream velocity of $U_\infty = 30$ m/s, corresponding to a chord-based Reynolds number of $Re_c = 7.0 \times 10^5$. The results are shown for the selective Strouhal numbers based on the narrowband peaks observed at the far-field spectral levels in Fig. 12. At first glance, it is evident that the application of the H-SCF and SCF does not influence the overall directivity shape for the presented range of Strouhal numbers compared to the Baseline case. For $\alpha = 14°$, at f_1, the acoustic amplitude of the directivity results remains unchanged for the H-SCF and SCF configurations compared to the Baseline case but a reduction of up to 10 dB is observed at $\alpha = 18°$ for the SCF configuration over the whole polar angles. The reduction in the spectral levels for the cove filler configurations for the peaks $f_{2\&4}$ are substantial, with a reduction of up to 20 dB at both the presented angles of attack. The noise level results show a significant reduction for the H-SCF and SCF cases relative to that of the Baseline case at $\alpha = 18°$, at all frequencies.

The overall sound pressure levels (OASPL) for the different configurations are shown in Fig. 17. The overall sound pressure level was resolved for a frequency range from $f = 100$ Hz to 32 kHz. The results show that the applications of the H-SCF and SCF reduce the overall noise level by about 2-3 dB at $\alpha = 14°$ and a significant reduction of up to 10 dB at the higher angles of attack ($\alpha = 18°$) compared to that of the Baseline case, particularly at locations upstream of the slat trailing edge.

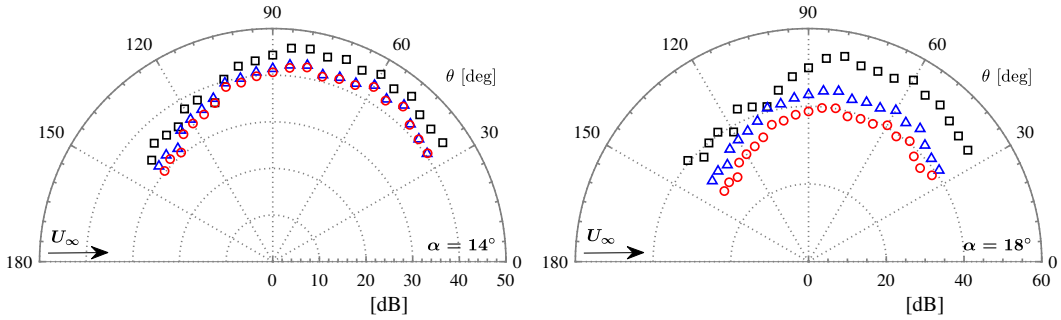

Fig. 17. Overall sound pressure level calculated from the far-field microphones, for Baseline □, H-SCF △ and SCF ○.

IV. Conclusion

The aerodynamic and aeroacoustic performance of 30P30N airfoil was tested at the University of Bristol aerodynamic and aeroacoustic test facilities. The aerodynamic lift and drag measurements have shown an insignificant difference between the tested configuration. The H-SCF showed superior aerodynamic performance compared to the Baseline, H-SCF, and SCF configuration in terms of the C_L/C_D and the drag-polar plots. The C_p distribution shows very similar characteristics between all the tested configurations. However, the suction peak for the H-SCF/SCF configurations was increased by up to 20% on the main-element and 5% on the flap relative to the Baseline case. The near-field measurements accurately captured the characteristic slat tonal behavior for the Baseline case. This tonal behavior was eliminated by the use of the H-SCF and the SCF. The near-field surface pressure measurements show increased noise at low frequency for the H-SCF and SCF compared to the Baseline case. However, this increase in low-frequency spectra was not observed in the far-field measurements this identifies the increased spectra to the non-propagating hydrodynamic energy field within the slat and main-element region. The far-field noise spectra measured above the slat trailing edge showed a reduction in the noise levels by up to 5-9 dB for the H-SCF and SCF relative to the Baseline case. The near- to far-field coherence results showed high coherence between the tonal peaks for the Baseline case and it also showed high coherence for the broadband spectra for the SCF configuration. The auto-correlation for the surface microphones showed slow decaying periodic behavior for the Baseline case with high amplitude, whereas, for the H-SCF and SCF configuration the results exhibited fast decaying periodic behavior with much lower amplitude. The slow decaying periodic behavior for the Baseline case is indicative of vortex shedding and the vortex shedding frequency was found to be the same as that of the strongest tonal peak observed in the near- and far-field measurements. The directivity calculated from the far-field microphones were also presented at selective frequencies and the results showed a reduction of up to 20 dB at the tonal frequencies for the H-SCF and SCF configuration. The OASPL show that the application of H-SCF and SCF reduces the noise levels by 2-3 dB relative to the Baseline case.

References

[1] Kamliya Jawahar, H., Azarpeyvand, M., and Carlos R.Ilario., "Aerodynamic and Aeroacoustic Performance of Three-element High Lift Airfoil fitted with Various Cove Fillers", AIAA 2018-3142, 2018.

[2] Kamliya Jawahar, H., Showkat Ali, S. A., Azarpeyvand, M., and Carlos R.Ilario., "Aeroacoustic Performance of Three-element High Lift Airfoil with Slat Cove Fillers", 25th AIAA/CEAS Aeroacoustic conference, Delft University of Technology, Netherlands, 2019.

[3] Kamliya Jawahar, H., Azarpeyvand, M., and Carlos R.Ilario. "Experimental Investigation of Flow Around Three-element High-lift Airfoil with Morphing Fillers", AIAA 2017-3364, 2017.

[4] Ai, Q., Kamliya Jawahar, H., and Azarpeyvand, M., "Experimental Investigation of Aerodynamic Performance of Airfoils Fitted with Morphing Trailing Edges", AIAA 2016-1563, 2016.

[5] Kamliya Jawahar, H., Ai, Q., and Azarpeyvand, M., "Experimental and Numerical Investigation of Aerodynamic Performance of Airfoils Fitted with Morphing Trailing Edges", AIAA 2017-3371, 2017.

[6] Kamliya Jawahar, H., Azarpeyvand, M., and Silva, C., "Aerodynamic and Aeroacoustic Performance of Airfoils Fitted with Morphing Trailing-edges", AIAA 2018-2815, 2018.

[7] Kamliya Jawahar, H., Ai, Q., and Azarpeyvand, M., "Experimental and Numerical Investigation of Aerodynamic Performance of Airfoils with Morphed Trailing Edges", *Renewable Energy*, Vol. 127, 2018, pp. 355-367.

[8] Liu, H.R., Azarpeyvand, M., Wei, J.J., and Qu, Z.G., "Tandem Cylinder Aerodynamic Sound Control Using Porous Coating", *Journal of Sound and Vibration*, Vol. 334, 2015, pp. 190-201.

[9] Showkat Ali, S. A., Azarpeyvand, M., and Ilario, C., "Trailing Edge Flow and Noise Control using Porous Treatments", *Journal of Fluid Mechanics*, Vol. 850, 2018, pp. 83-119.

[10] Showkat Ali, S. A., Szoke, M., Azarpeyvand, M., and Ilario, C., "Turbulent Flow Interaction with Porous Surfaces", AIAA 2018-2801, 2018.

[11] Showkat Ali, S. A., Azarpeyvand, M., Szoke, M. and da Silva, C. R. I., "Boundary layer flow interaction with a permeable wall," *Physics of Fluids*, Vol. 30, 2018, pp. 085111.

[12] Afshari, A., Azarpeyvand, M., Dehghan, A. A., and Szoke, M., "Trailing Edge Noise Reduction Using Novel Surface Treatments", AIAA 2016-2834, 2016.

[13] Liu, X., Kamliya Jawahar, H., Azarpeyvand, M., and Theunissen, R. "Aerodynamic Performance and Wake Development of Airfoils with Serrated Trailing Edges", *AIAA Journal*, Vol. 55, No. 11, 2017, pp. 3669-3680.

[14] Lyu, B., Azarpeyvand, M., and Sinayoko, S., "Prediction of Noise from Serrated Trailing Edges", *Journal of Fluid Mechanics*, Vol. 793, 2016, pp. 556-588.

[15] Mayer, Y. D., Lyu, B., Kamliya Jawahar, H., and Azarpeyvand, M., "A Semi-analytical Noise Prediction Model for Airfoils with Serrated Trailing Edges", *Renewable Energy (in press)*, 2019.

[16] Szoke, M., Fiscaletti, D., and Azarpeyvand, M., "Effect of Inclined Transverse Jets on Trailing-edge Noise Generation," *Physics of Fluids*, Vol. 30, 2018, pp. 085110.

[17] Roger, M., and Perennes, S., "Low-Frequency Noise Source in Two Dimensional High-lift Devices", AIAA 2000-1972, 2000.

[18] Kolb, A., Faulhaber, P., Drobietz, R., and Grunewald, M., "Aeroacoustic Wind Turbine Measurements on a 2D High-lift Configuration", AIAA 2007-3447, 2007.

[19] Mendoza, J.M., Brooks, T.F., and Humphreys, W.M., "An Aeroacoustic Study of a Leading Edge Slat Configuration", *international Journal of Aeroacoustics*, Vol. 1, No. 3, 2002, pp. 241-274.

[20] Hein, S., Hohage, T., Koch, W., and Schoberl, J., "Acoustic Resonances in a High-lift Configuration", *Journal of Fluid Mechanics*, Vol. 582, pp: 179-202, 2007.

[21] Makiya, Sanehiro., Inasawa, A., and Asai, M., "Vortex Shedding and Noise Radiation from a Slat Trailing Edge", *AIAA Journal*, Vol. 48, No. 2, 2010, pp: 502-508.

[22] Terracol, M., Manoha, E., and Lemoine, B., "Investigation of the Unsteady Flow and Noise Generation in a Slat Cove", *AIAA Journal*, Vol. 54, No. 2, 2016, pp: 469-489.

[23] Pagani, C. C., Souza, D. S., and Medeiros, M. F., "Slat Noise: Aeroacoustic Beamforming in Closed-Section Wind Tunnel with Numerical Comparison", *AIAA Journal*, Vol. 54, No. 7, 2016, pp: 2100-2115.

[24] Pagani, C. C., Souza, D. S., and Medeiros, M. F., "Experimental Investigation on the Effect of Slat Geometrical Configuration on Aerodynamic Noise", *Journal of Sound and Vibration*, Vol. 394, pp: 256-279, 2017.

[25] Pascioni, K. A., and Cattafesta, L. N., "An Aeroacoustic Study of a Leading-edge Slat: Beamforming and Far-field Estimation using Near-field Quantities", *Journal of Sound and Vibration*, Vol. 429, pp: 224-244, 2018.

[26] Li, L., Liu, P., Guo, H., Hou, Y., Geng, X., and Wang, J., "Aeroacoustic Measurement of 30P30N High-lift Configuration in the Test Section with Kevlar Cloth and Perforated Plate", *Aerospace Science and Technology*, Vol. 70, pp: 590-599, 2017.

[27] Li, L., Liu, P., Guo, H., Geng, X., Hou, Y., and Wang, J., "Aerodynamic and Aeroacoustic Experimental Investigation of 30P30N High-lift Configuration", *Applied Acoustics*, Vol. 132, pp: 43-48, 2018.

[28] Li, L., Liu, P., Xing, Y., and Guo, H., "Time-frequency Analysis of Acoustic Signals from a High-lift Configuration with two Wavelet Functions", *Applied Acoustics*, Vol. 129, pp: 155-160, 2018.

[29] Li, L., Liu, P., Xing, Y., and Guo, H., "Wavelet Analysis of the Far-Field Sound Pressure Signals Generated from a High-lift Configuration", *AIAA Journal*, Vol. 56, No.1 pp: 432-437, 2018.

[30] Horne, W. C., James, K. D., Arledge, T. K., Soderman, P. T., Field, M., Burnside, N., and Jaeger, S. M., "Measurement of 26%-scale 777 Airframe Noise in the NASA Ames 40- by 80 foot Wind Tunnel", AIAA 2005-2810, 2005.

[31] Streett, C., Casper, J., Lockard, D., Khorrami, M., Stoker, R., Elkoby, R., Wenneman, W., and Underbrink, J., "Aerodynamic Noise Reduction for High-Lift Devices on a Swept Wing Model", AIAA 2006-212, 2006.

[32] Andreou, C., Graham, W., Shin, H.C., Street, T., Member, S., and Lecturer, S., "Aeroacoustic study of airfoil leading edge high-lift devices", AIAA 2006-2515, 2006.

[33] Andreou, C., Graham, W., Shin, H.-c., Introduction, I., Street, T., Member, S., and Lecturer, S., "Aeroacoustic Comparison of Airfoil Leading Edge High-Lift Geometries and Supports", AIAA 2007-230, 2007.

[34] Murayama, M., Nakakita, K., Yamamoto, K., Ura, H., and Ito, Y., "Experimental Study of Slat Noise from 30P30N Three-Element High-Lift Airfoil in JAXA Hard-Wall Low-Speed Wind Tunnel", AIAA 2014-2080, 2014.

[35] Imamura, T., Ura, H., Yokokawa, Y., Enomoto, S., Yamamoto, K., Hirai, T., Group, A. P., and Division, E. S., "Designing of Slat Cove Filler as a Noise Reduction Device for Leading-edge Slat", AIAA 2007-3473, 2007.

[36] Ura, H., Yokokawa, Y., Imamura, T., Ito, T., and Yamamoto, K., "Investigation of Airframe Noise from High Lift Configuration Model", AIAA 2008-19, 2008.

[37] Shmilovich, A., Yadlin, Y., and Pitera, D. M., "Wing Leading Edge Concepts for Noise Reduction", 27th International Congress of the Aeronautical Sciences (ICAS), 2010.

[38] Shmilovich, A., Yadlin, Y., and Company, T. B., "High-lift systems for enhanced take-off performance", 28th International Congress of the Aeronautical Sciences, 2012, pp. 1-13.

[39] Scholten, W. D., Hartl, D. J., Turner, T. L., and Kidd, R. T., "Development and Analysis-Driven Optimization of Superelastic Slat-Cove Fillers for Airframe Noise Reduction", *AIAA Journal*, dec 2015, pp. 1-17.

[40] Tao, J. and Sun, G., "A Novel Optimization Method for Maintaining Aerodynamic Performances in Noise Reduction Design", Aerospace Science and Technology, Vol. 43, 2015, pp. 415-422.

[41] Mayer, Y., Kamliya Jawahar, H., Mate, S., and Azarpeyvand, M., "Design of an Aeroacoustic Wind Tunnel Facility at the University of Bristol", AIAA 2018-3138, 2018.

[42] Garcia-Sagrado, A. and Hynes, T., "Wall-Pressure Sources Near an Airfoil Trailing Edge Under Separated Laminar Boundary Layers", *AIAA Journal*, Vol. 49, No. 9, 2011, pp. 1841-1856.

[43] Garcia-Sagrado, A. and Hynes, T., "Stochastic Estimation of Flow near the Trailing Edge of a NACA0012 Airfoil", *Experiments in Fluids*, Vol. 51, No. 4, 2011, pp. 1057-1071.

[44] Garcia-Sagrado, A. and Hynes, T., "Wall Pressure Sources Near an Airfoil Trailing Edge under Turbulent Boundary Layers", *Journal of Fluids and Structures*, Vol. 30, 2012, pp. 3-34.

[45] Valarezo, W. O., "High-lift testing at high Reynolds numbers", AIAA-92-3986, 1992.

[46] Valarezo, W. O., Dominik, C. J., and Mcghee, R. J., "Reynolds and Mach number effects on Multielement Airfoils", N93-27446, 1992.

[47] Chin, V. D., Peters, D.W., Sdaid, F.W., and Mcghee, R. J., "Flowfield Measurements About a Multi-Element Airfoil At High Reynolds Numbers", AIAA-93-3137, 1993.

[48] Olson, S., Thomas, F., and Nelson, R., "A Preliminary Investigation into Slat Noise Production Mechanisms in a High-lift Configuration", AIAA 2000-4508, 2000.